JOURNAL OF SPACECRAFT AND ROCKETS
Vol. 32, No. 1, January–February 1995

Direct Simulation Monte Carlo Calculation of a Jet Interaction Experiment

Paul V. Tartabini,* Richard G. Wilmoth,† and Didier F. G. Rault†
NASA Langley Research Center, Hampton, Virginia 23681

This study deals with the development of a methodology for numerically simulating the interaction of a reaction control system (RCS) jet with a low-density external flow. A European Space Agency experiment was chosen as a test case, since it provided experimental data that could validate some of the numerical results. The initial approach was to focus on several subproblems having direct relevance to the full interaction problem. This enabled different numerical methods to be investigated separately and validated for each part of the interaction problem. In this manner, the best methodology for solving the full interaction problem was developed. The subproblems considered in this study included typical RCS nozzle and plume flows, a flat plate at zero incidence, and the flow past the experimental test model without the control jet firing. Once these calculations were completed, a simulation was performed of the test model with the control jet operating at the experimental density. The results from this final simulation were compared with experimental measurements.

Nomenclature

d_{ref}	= reference diameter, m
Kn_{throat}	= Knudsen number at nozzle throat
Kn_{lip}	= Knudsen number at nozzle lip
M	= Mach number
n	= number density, molecules/m^3
n_∞	= freestream number density, molecules/m^3
P	= pressure, Pa
Re	= Reynolds number
T_{ref}	= reference temperature, K
T_{wall}	= temperature of nozzle wall
T_∞	= freestream temperature, K
X, Y, Z	= Cartesian body coordinates
ρ	= density, kg/m^3
ρ_∞	= freestream density, kg/m^3

Introduction

MOST space vehicles are controlled with reaction thrusters during atmospheric entry. These reaction control system (RCS) jets are used independently or in conjunction with movable aerodynamic surfaces, depending on the specific vehicle configuration and flight conditions. The exhaust plumes of these control jets act as barriers to the external flow, creating an effect that can change the pressure distribution along the vehicle surface containing the jet, as well as on surfaces surrounding the exhaust plume.[1] These surface pressure perturbations lead to interaction forces which must be accurately predicted in order to obtain the desired vehicle performance. The use of RCS jets becomes vital at higher altitudes where the density is low enough to render the control surfaces ineffective. As the altitude increases and the freestream flow becomes more rarefied, the level of interaction between the control jet and the freestream diminishes and is practically nonexistent when the freestream mean free path is very large.[2] Therefore it is crucial to accurately model RCS firings at intermediate altitudes where reaction controls are needed and significant control-jet interactions are expected.

Received Aug. 5, 1993; revision received April 7, 1994; accepted for publication April 14, 1994.

*Aero-Space Technologist, Aerothermodynamics Branch, Space Systems Division. Member AIAA.

†Senior Research Engineer, Aerothermodynamics Branch, Space Systems Division. Senior Member AIAA.

It is usually not possible to match the similarity parameters necessary to realistically model an RCS plume interaction in a wind tunnel, because of the complex vehicle geometry and varying flight conditions along the trajectory.[3] Indeed, flight-test results from the first Shuttle flights showed that the control-jet interaction effect could not be adequately predicted from wind-tunnel tests alone.[1] Furthermore, the flight conditions encountered during early entry were much more rarefied than the conditions that were used in wind-tunnel simulations. Consequently, an empirical approach was taken in the Shuttle program through a series of studies conducted during later flights. Correlation parameters extracted from flight data and previous wind-tunnel tests proved adequate to account for plume interaction effects throughout the orbiter's trajectory. Twelve years after the first Shuttle flight, the interaction effects are well known but little understood. It is still not possible to accurately predict the RCS plume freestream interaction for a general body shape from orbit to landing. Clearly, a necessary step in the design process of a future vehicle will include a realistic assessment of the RCS plume interaction with the freestream flow throughout the entire re-entry trajectory.

In an effort to gain further insight into the control-jet interaction problem, an experimental study was conducted by the European Space Agency (ESA) at the SR3 low-density wind tunnel in Meudon, France. The test model shown in Fig. 1 was composed of two perpendicular flat plates with sharp leading edges aligned parallel to a Mach-20 nitrogen flow. This simple corner geometry was used to isolate critical jet interaction areas on complex bodies. A nitrogen control jet was fired from the horizontal plate at several different momentum flux values. Wall pressures were measured with external pressure transducers at various stations on both plates. Although the model was tested at several different freestream flow conditions, only the most rarefied case is studied in this paper. The external flow conditions are shown in Table 1.

The ultimate objective of this research is to provide a methodology for numerically simulating control jet interactions with low-density flows. The initial approach is to focus on several subproblems, each of which has direct relevance to solving a full RCS interaction problem (Fig. 2). The purpose of this approach is to separately investigate and validate the numerical methods required for the subproblems in order to develop the best methodology for solving the full interaction problem. In these initial studies, both continuum and noncontinuum techniques are used. The continuum method is the viscous nozzle analysis program (VNAP2) of Cline,[4] which numerically solves the Navier-Stokes equations for two-dimensional or axisymmetric flows. The noncontinuum method is the direct simulation Monte Carlo (DSMC) method of Bird,[5] which is well suited for simulating rarefied flows.

Table 1 Experimental flow conditions

Stagnation temperature, T_0	1110 K
Stagnation pressure, P_0	3.5 bars
Freestream density, ρ_∞	1.7×10^{-5} kg/m^3
Freestream velocity, U_∞	1502 m/s
Freestream, temperature, T_∞	13.3 K
Freestream Mach number, M_∞	20.2
Freestream Reynolds number, Re_∞	285 cm^{-1}
Static pressure, P_s	0.067 Pa
Dynamic pressure, q	19.2 Pa
Knudsen number, Kn	0.017

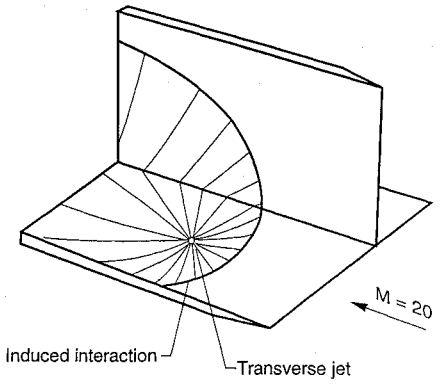

Fig. 1 Test model for ESA corner-flow–jet interaction.

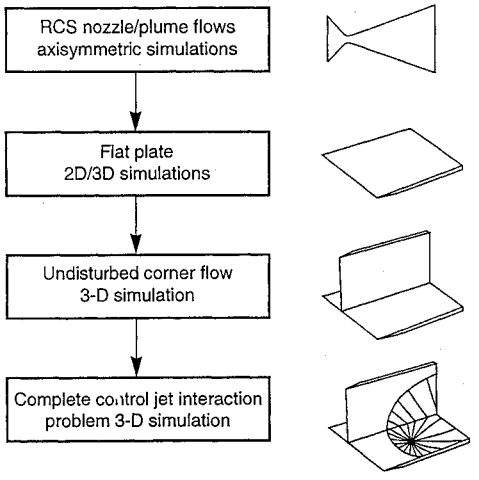

Fig. 2 Outline of numerical solution procedure followed in this paper.

The rest of this paper is divided into six sections. The next section contains a brief description of the three numerical codes used in this study. Then a methodology is presented for solving internal nozzle and external plume flows of typical RCS thrusters, and results are presented for two nozzle geometries, including the one from the control-jet interaction experiment. The next section presents two-dimensional and three-dimensional DSMC simulations of the flow over a flat plate with the same leading-edge geometry and freestream conditions as the ESA experiment. The section after that contains results of three-dimensional DSMC simulations of the full ESA test model without the control jet; these undisturbed corner flow results are compared with wind-tunnel measurements. Finally, results are presented from a three-dimensional DSMC simulation of the ESA test model with the control jet turned on. The last section summarizes the results.

Computational Tools

Due to the expanding nature of RCS plumes, a wide range of Knudsen numbers is encountered in this study. These large expansions, combined with the three-dimensional complexities of the ESA experiment, require the use of a series of CFD simulation codes. First, continuum flows are simulated with the VNAP2 code. This code is a time-dependent, finite-difference, full-Navier-Stokes-equation solver for two-dimensional planar and axisymmetric geometries. VNAP2 uses the explicit two-step MacCormack method and is capable of calculating laminar and turbulent viscous flows.

In addition, the DSMC method is used to compute flowfields in the transitional flow regime. Both two-dimensional and three-dimensional DSMC codes are used in various parts of the study. In both DSMC codes, molecular collisions are modeled using the variable hard sphere (VHS) molecular model,[6] and the energy exchange between the kinetic and internal modes is handled with the Larsen-Borgnakke statistical model.[7] The freestream viscosity and mean free path are computed using the VHS collision model for nitrogen with $T_{\text{ref}} = 300$ K, $d_{\text{ref}} = 4.07 \times 10^{-10}$ m, and a temperature exponent of the viscosity coefficient of 0.75. The gas-surface interactions are assumed to be fully diffuse with full momentum and energy accommodation.

The generalized two-dimensional axisymmetric DSMC code was developed by Bird and is known as the G2 code.[8] This code is used in the nozzle-plume and flat-plate simulations. The DSMC simulations of the corner flow and the control-jet interaction are done with a three-dimensional DSMC code that was devised by Bird[9] and further developed by Rault.[10] The main difference between the two-dimensional and three-dimensional DSMC codes is the construction of computational grids. The three-dimensional code utilizes an unstructured Cartesian grid, whereas the G2 code uses a body-fitted block-structured grid.

RCS Nozzle and Plume Simulations

A realistic simulation of a control-jet interaction requires an accurate description of the RCS jet. Therefore, the initial task is the development and testing of a methodology for solving internal nozzle and external plume flows of typical RCS thrusters. Two nozzles are selected for this study. The first one, referred to as the Lewis nozzle, is chosen because it has been tested both experimentally and computationally. Internal nozzle calculations are performed using both Navier-Stokes and DSMC techniques, and the results are compared with previously published data. A similar numerical approach is applied to simulate the flowfield within the second nozzle, namely the ESA nozzle.

Lewis Nozzle

Axisymmetric simulations are performed for a nozzle tested at the NASA Lewis Research Center. Extensive computational and experimental results have been published for this nozzle by Boyd, Penko, and various co-authors.[11–14] Results presented here are from nozzle simulations of conditions given in Table 2. The VNAP2 simulations are started upstream of the nozzle throat, using the given stagnation conditions, and extended to the exit plane. Laminar flow is assumed, and the viscosity is computed to give the same viscosity-temperature relationship as that used in the DSMC simulations. A computational grid divided into 41 radial and 81 axial grid lines is used. The exit-plane boundary condition is extrapolated from interior points of the nozzle. A no-slip boundary condition is enforced at the wall, which is modeled as isothermal with a temperature of 545 K.

The DSMC simulations are started at the nozzle throat using velocity, density, and temperature profiles from the VNAP2 solution. The simulation is extended into the near-field portion of the plume, and a vacuum boundary condition is imposed on the outer plume boundaries. The computational domain consists of 26,000 numerical

Table 2 RCS nozzle geometry and flow conditions

	Lewis nozzle	ESA nozzle
Throat and exit diameters, mm	3.18, 31.8	0.213, 1.53
Divergent half angle, deg	20	9
Gas	N_2	N_2
Stagnation pressure, Pa	6.4×10^3	4.0×10^7
Stagnation temperature, K	699	300
Re_{throat}	850	3200
Kn_{throat}	0.001	4.7×10^{-5}
Kn_{lip}	0.100	3.2×10^{-3}

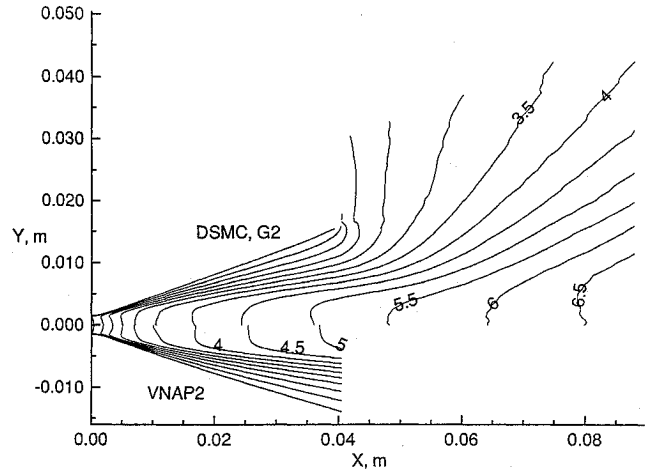

Fig. 3 Comparison of computed DSMC and VNAP2 Mach-number contours within the Lewis nozzle.

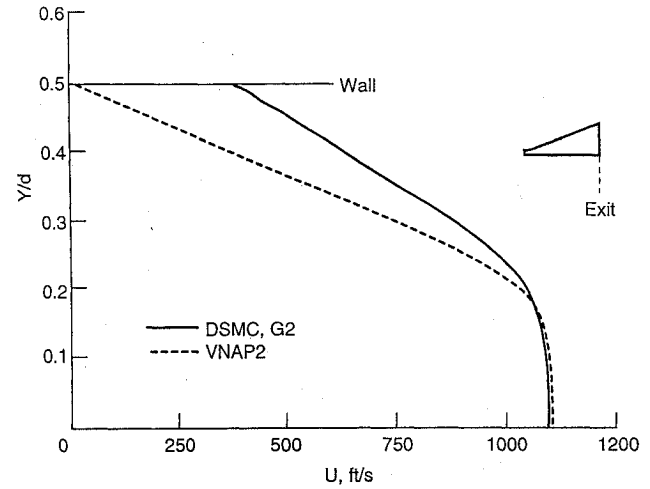

Fig. 4 Comparison of computed DSMC and VNAP2 exit velocity profiles for the Lewis nozzle.

cells. Some of the cells in the core of the nozzle near the throat exceed one mean free path in length. These cells are small, however, compared with local density-gradient scales.

A comparison of the two numerical solutions is presented in Fig. 3, where the upper half of the nozzle shows Mach-number contours generated with DSMC and the bottom half shows contours computed with VNAP2. Both solutions indicated that the boundary layer along the nozzle wall is thick, which is expected in a viscous, low-Reynolds-number flow. Also, both codes give nearly the same solution in the low-Knudsen-number region of the nozzle near the throat. Here the gas behaves as a continuous fluid and is in thermal equilibrium. The two solutions begin to disagree in the rarefied regions near the exit, especially in the areas surrounding the nozzle lip. There are two primary reasons for these differences in the computed results. First, the no-slip boundary condition imposed by VNAP2 is unrealistic for the transitional flow found in the vicinity of the nozzle exit. Second, the extrapolated exit boundary condition imposed on the VNAP2 solution makes it impossible for the subsonic flow in the boundary layer to sense the low back pressure. Consequently, the boundary-layer flow does not accelerate and the Mach contours remain parallel to the wall. These imprecise boundary conditions have a relatively small effect except in the vicinity of the lip. Furthermore, these effects are negligible near the throat of the nozzle, which validates the use of the VNAP2 throat profile as a start line for the DSMC calculation. Finally, the DSMC results presented here provide a better match to the VNAP2 results along the nozzle centerline than the computational results shown in Ref. 11.

The effect of flow rarefaction is evident in Fig. 4, which shows the axial velocity profile in the exit plane. The radial distance is nondimensionalized by the exit diameter. The DSMC solution predicts a significant velocity slip at the nozzle lip, whereas the VNAP2 results show the imposed no-slip behavior. Also, the DSMC results from the present simulations match the VNAP2 results in the core of the nozzle better than the DSMC results shown in Ref. 14. There are differences in the temperature exit profiles (see Fig. 5) calculated by the two codes. Translational and rotational temperatures are computed with the DSMC code, since a diatomic test gas is used. The VNAP2 calculation, however, assumed thermal equilibrium; thus only one thermodynamic temperature is shown. The DSMC results indicate that the flow is in thermal nonequilibrium at the exit, since the two temperatures differ slightly throughout the exit plane. Furthermore, there is a significant jump between the temperature of the wall and the flow immediately adjacent to the wall. The VNAP2 results exhibit the imposed isothermal boundary condition. Although the temperature jump predicted here is similar to that predicted by the DSMC results in Ref. 14, there are differences between the two DSMC solutions in the degree of thermal nonequilibrium near the nozzle wall in the exit plane.

As a check of the numerical simulations, a comparison is made between computed and measured pitot pressures. The computed pressures are converted to the pressure behind a normal shock using the Rayleigh pitot-tube equation to account for the total pressure loss through the shock in front of the experimental pitot probe.[15] Figure 6 shows the measured pitot pressure in the exit plane along with the pitot pressures calculated using both numerical codes. Clearly the DSMC results provide a more realistic physical description of the flow.

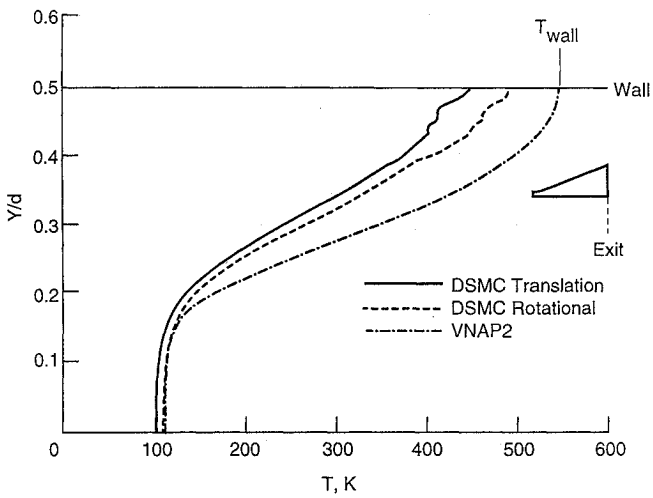

Fig. 5 Comparison of computed DSMC and VNAP2 exit temperature profiles for the Lewis nozzle.

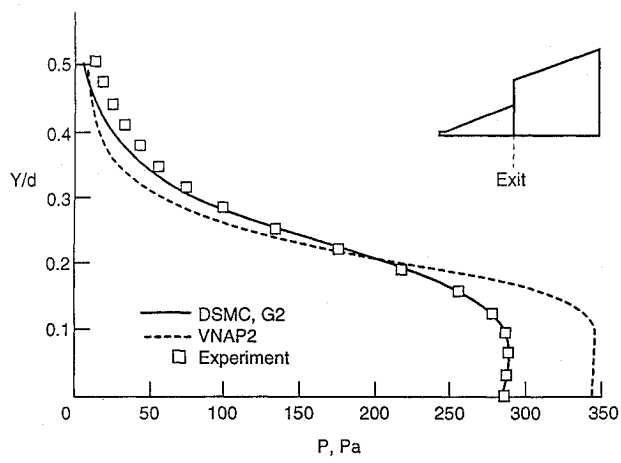

Fig. 6 Measured and computed pitot pressures in the exit plane of the Lewis nozzle.

ESA Nozzle

The initial validation provided by the Lewis nozzle simulations demonstrates that VNAP2 provides an accurate description of a low-density nozzle flowfield, especially in the regions of the flow that are in thermal equilibrium. Therefore, since the ESA nozzle operated at a higher Reynolds number than the Lewis nozzle and the stagnation pressure was 4 orders of magnitude higher (Table 2), VNAP2 is used to compute the internal nozzle flow. Subsequently, the exit plane from the VNAP2 solution is used as an inflow boundary condition for a DSMC simulation of the external plume flow. This approach was taken in order to avoid the high computational cost associated with a DSMC simulation of the internal flow. The throat and exit Knudsen numbers (Table 2) indicate that the internal flow was almost entirely in the continuum regime, with the flow at the exit just approaching transitional conditions. Therefore, the degree of thermal nonequilibrium will be minimal, thus validating the use of the VNAP2 exit plane as a startline for the DSMC simulation. Figure 7 shows Mach-number contours of the internal flow obtained from the VNAP2 simulation. The boundary layer is thinner than in the Lewis nozzle because of the higher Reynolds number.

The plume flow is characterized by extreme variations in density due to the rapid expansion of the internal flow into a near-vacuum. Because of the requirement that the simulation scale factors for molecular flux must remain the same in all parts of the computational domain, a satisfactory time increment in the core region of the plume provided a restrictively small increment for larger cells in the plume farfield. In order to avoid a large convergence time brought about by a significant time-step disparity, the DSMC plume simulation is split into two parts. First, the plume core, which is essentially continuum flow, is defined as the region where the Bird breakdown parameter[16] is less than 0.04. This part of the solution was obtained with a DSMC simulation of a region large enough to contain this breakdown contour. Since the flow within this region is in thermal equilibrium, it is appropriate to extract flow properties along the 0.04 breakdown contour of the DSMC solution and use them as inflow to a separate DSMC simulation of an outer region describing the plume farfield.

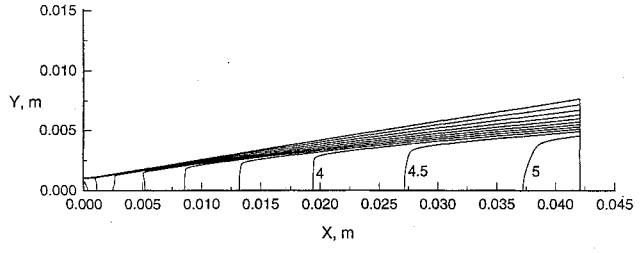

Fig. 7 Computed VNAP2 Mach-number contours in the ESA nozzle.

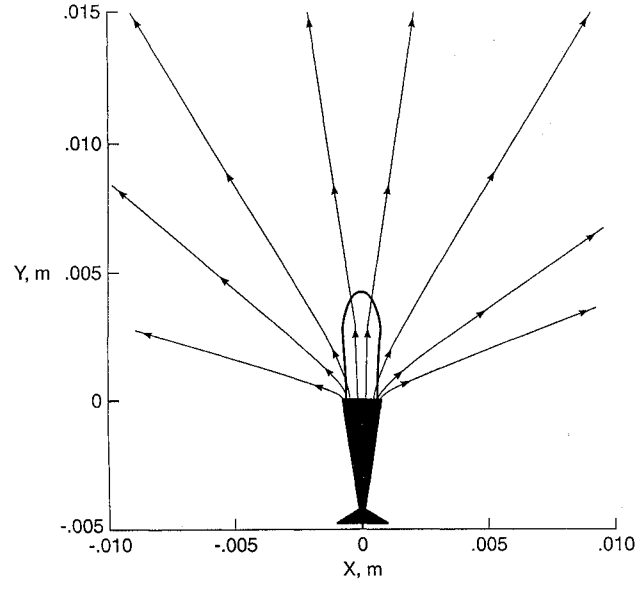

Fig. 8 Computed DSMC velocity steamlines and the 0.04 breakdown parameter contour in the plume of the ESA nozzle.

Results from the DSMC plume simulations are shown in Fig. 8. A solid wall perpendicular to the exit plane is included to approximate the ESA experiment; however, no external freestream flow is imposed. The wall temperature is assumed to be 300 K. The solid line is the 0.04 Bird breakdown contour, and the lines with arrows are streamlines. In this computational domain, which is only about 10 by 10 exit diameters in size, the density varies by 5 orders of magnitude. The rapid expansion is also demonstrated by the large turning of the flow at the nozzle lip as shown by the streamlines.

No appropriate experimental data are available for comparison with these solutions. However, the results provide an initial assessment of the extent of the plume core and the range of density variations that can be expected in a three-dimensional DSMC simulation of the full ESA experiment. From this solution, the best way to model the jet in the full simulation can be determined.

Flat-Plate Simulations

As a first step to computing the full geometry associated with the ESA experiment, a calculation is carried out on a beveled horizontal plate at the freestream conditions given in Table 1. The plate is 120 mm long and 6 mm thick with a 20-deg bevel, essentially the same as the horizontal plate containing the jet in the experimental test model. This case presents an opportunity to compare the three-dimensional and two-dimensional DSMC algorithms. In addition, this flat-plate simulation serves as a baseline to assess the effect of the vertical plate on the undisturbed corner flow.

In order to make a valid comparison between the two-dimensional and three-dimensional DSMC codes, the computational domain used in the three-dimensional simulation is modified so that end effects do not change the two-dimensional nature of the flow. This was done by imposing specular boundary conditions on end planes perpendicular to the plate and parallel to the external flow. It is difficult to compare the size of the grids directly, since one has an added dimension; however, the grids gave approximately equal resolution in the streamwise and vertical directions.

Figures 9 and 10 show the density and temperature profiles, respectively, in planes perpendicular to the plate at locations of 40, 60, 80, and 100 mm from the leading edge. The density and temperature are nondimensionalized with the corresponding freestream values. Figure 9 indicates reasonably good agreement between the density profiles predicted by the two solutions. Both codes predict a thick and diffuse shock layer, the peak densities computed by G2 being about 10% higher than those predicted by the three-dimensional code. The difference was most likely due to grid differences between the three-dimensional code (unstructured grid) and the G2 code (block-structured grid). This same level of agreement is shown in Fig. 10 for the translational temperature. Both solutions show that the temperature of the flow adjacent to the wall decreases along the length of the plate with considerable temperature jump ($T_{\text{wall}}/T_\infty = 22.6$). The results in Fig. 10 show that the gas temper-

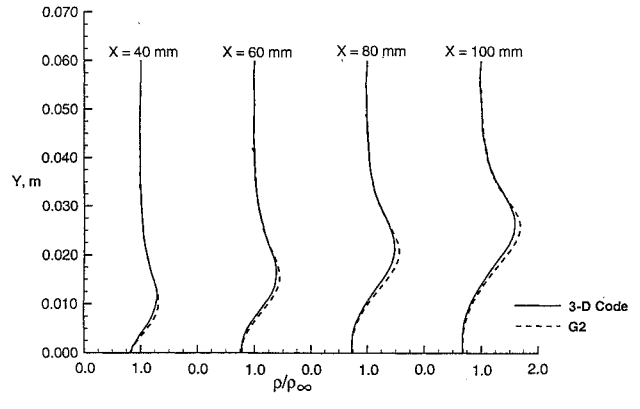

Fig. 9 Comparison of density profiles from the the 2-D and 3-D DSMC flat-plate simulations.

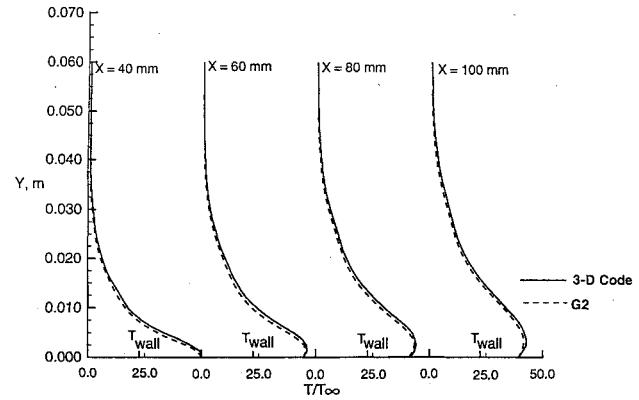

Fig. 10 Comparison of temperature profiles from the 2-D and 3-D DSMC flat-plate simulations.

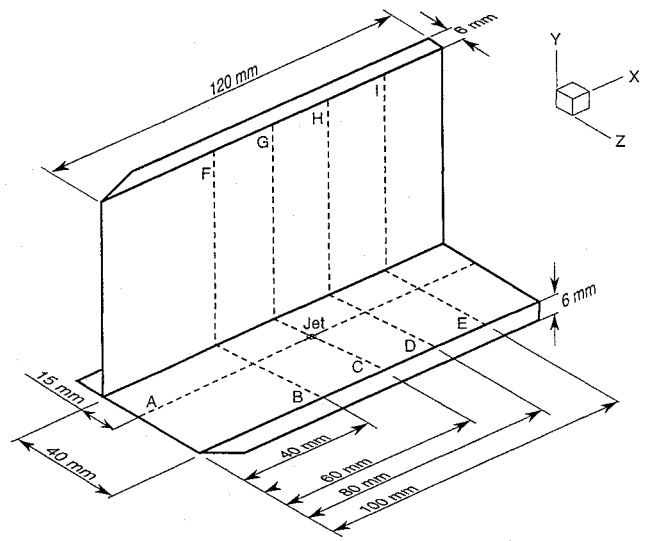

Fig. 11 Overall dimensions and pressure-orifice locations for the ESA experimental test model.

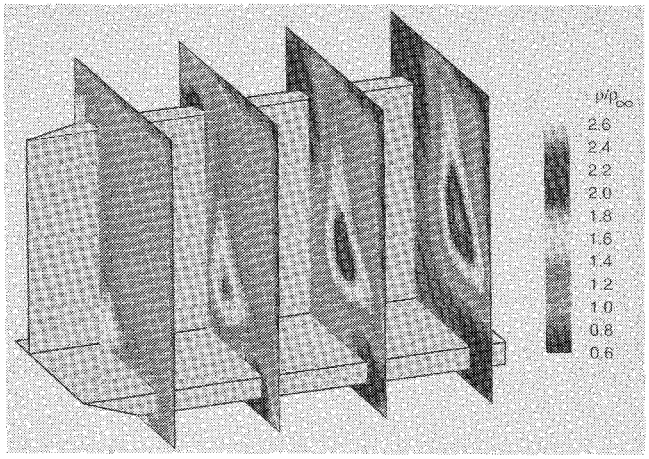

Fig. 12 Density contours around the undisturbed test model (no jet firing).

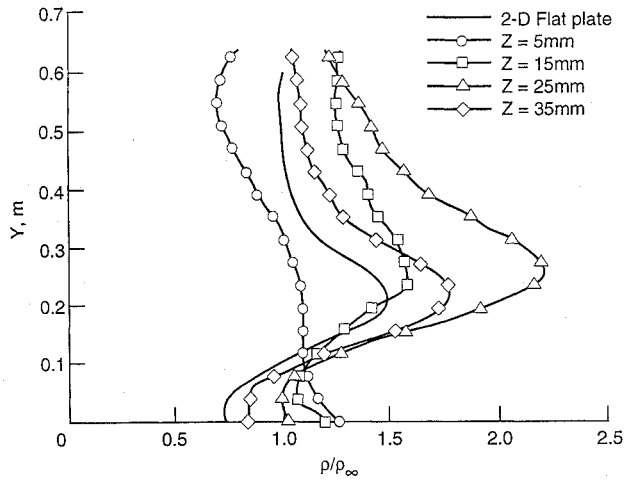

Fig. 13 Comparison of density profiles for the undisturbed corner flow and the flat plate at a location 80 mm from the leading edge.

ature near the plate exceeded the wall temperature by 200 to 400 K. In addition, both solutions show a velocity slip of 1100 m/s near the leading edge of the plate (not shown in the figures).

Simulations of Undisturbed Corner Flow

A three-dimensional simulation of the full test model without the jet is carried out at the freestream conditions listed in Table 1. The solution is compared with published wind-tunnel data from the ESA experiment.[17] Additionally, comparisons are made with the flat-plate simulations to determine the effect of the vertical wall on the flow structure. The dimensions of the test model are shown in Fig. 11, with the horizontal plate identical to the flat plate used in the previous section. The dashed lines on the model indicate nine sections along which surface pressures were measured in the experiment.

The general features of the flowfield are shown in Fig. 12 by density profiles in four planes normal to the X-axis at distances of 20, 50, 80, and 100 mm from the leading edge. The flow is characterized by a high-density region that begins in the corner at the leading edge of the model and extends outward equidistant from the two plates. This large density buildup is due to the intersection of the oblique shocks emanating from the leading edge of each plate. Further insight is gained by examining the development of the flowfield in the spanwise direction, that is, in a direction perpendicular to the vertical wall. Figure 13 shows the density profiles 80 mm from the leading edge at distances 5, 15, 25, and 35 mm from the vertical wall. Also, a density profile from the two-dimensional calculation at the same axial location is included for comparison. Clearly, the addition of the vertical plate significantly changes the flowfield due to the shock-shock intersection, which effectively compresses the freestream flow near the wall. Each spanwise profile indicates a higher density adjacent to the horizontal plate than in the two-dimensional flat-plate case. Also, the shock-layer thickness on the test model is substantially different from the flat-plate results. In addition, the intersection of the two shocks increases the peak density values at this axial location by 1.5 times over the two-dimensional flat-plate solution. Note that this peak density occurs 25 mm from the horizontal plate and 25 mm from the vertical plate. Finally, the density profile in the plane 35 mm from the vertical wall shows that the three-dimensional effects are beginning to diminish, since the shape of the density profile is approaching that of the two-dimensional profile.

The surface pressure distribution on the test model is shown in Fig. 14. The highest surface pressures are in the corner, where the density is higher. For comparison with experiment, surface pressures are extracted along the various sections of the test model indicated in Fig. 11. The test model had orifices connected to external pressure transducers placed along each of the sections. A comparison of the measured wall pressures along section A and the computed pressures is shown in Fig. 15. The pressure fluctuations in the computational profiles are due to the relatively large cells near the body and the way in which the profiles are extracted from the unstructured grid. For section A, the computed values exceed the measurements by up to 40%. The published experimental pressures were not corrected for orifice effects, which may be significant in transitional flows.[18] Therefore, an orifice correction factor is applied to the measurements, and the resulting corrected pressures are also plotted in this figure to give an estimate of the potential magnitude of the corrections. To perform the orifice corrections, an energy accommodation coefficient of 1.0 and an orifice temperature of 300 K are assumed. Further discussion of the sensitivity of these corrections

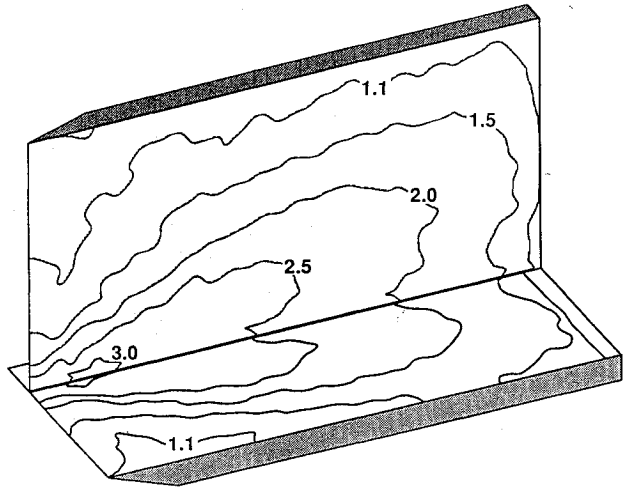

Fig. 14 Surface pressure distribution on the undisturbed test model (no jet firing).

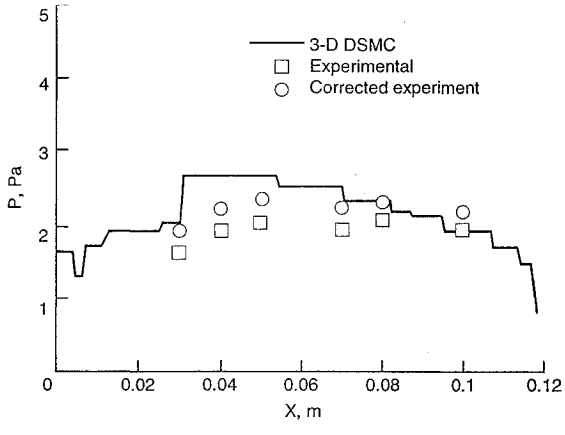

Fig. 15 Comparison of computed surface pressures with corrected and uncorrected measured wall pressures along section *A*.

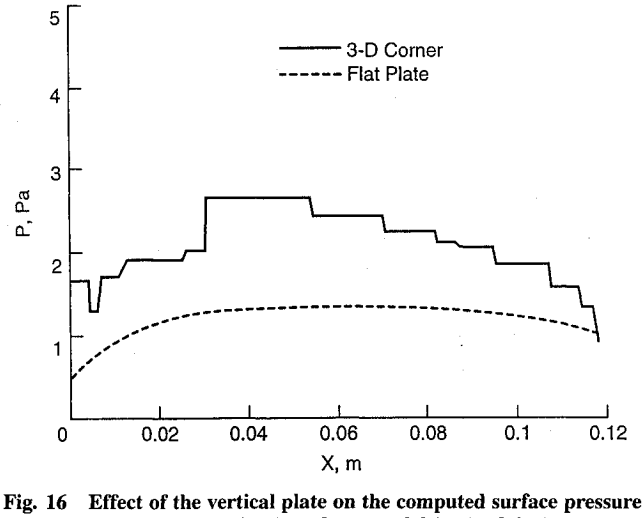

Fig. 16 Effect of the vertical plate on the computed surface pressure distribution along the undistributed test model (no jet firing).

to such assumptions is given in Ref. 18. Clearly the corrected experimental data provide a better match to the calculated results. Figure 16 compares the pressures predicted along section A for the undisturbed corner flow with the pressures predicted for the flat plate from the previous section. The pressure is higher for the corner flow because of the increase in density of the flow adjacent to the plate.

Figure 17 shows computed and measured surface pressure distributions on the horizontal plate along sections *B*,*C*,*D*, and *E*. Once

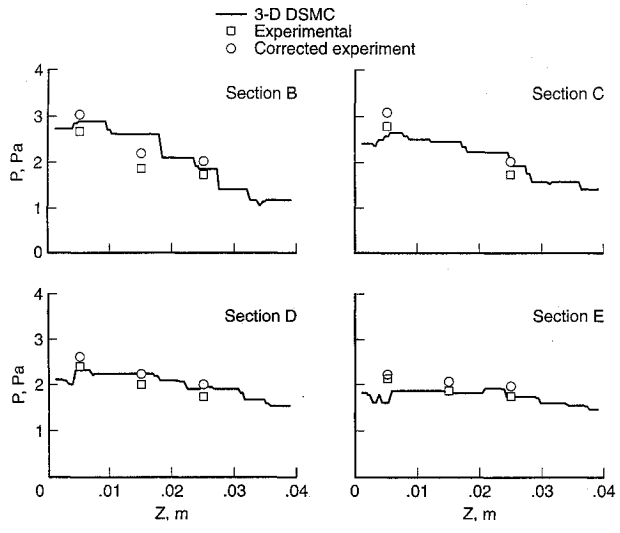

Fig. 17 Comparison of computed surface pressures with corrected and uncorrected measured wall pressures along the horizontal plate (sections *B–E*).

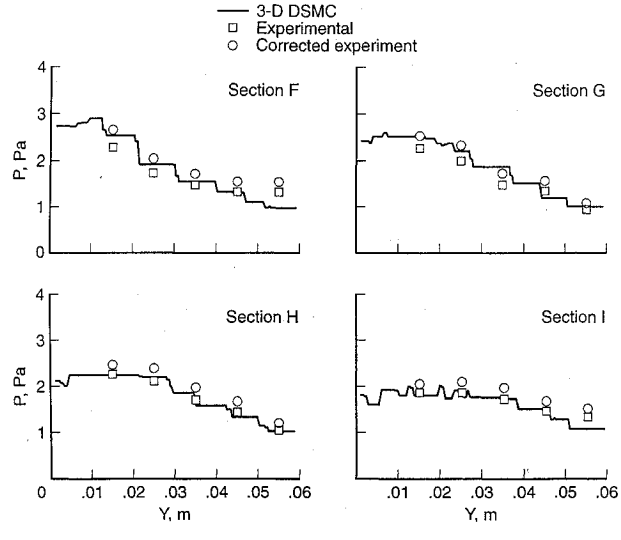

Fig. 18 Comparison of computed surface pressures with corrected and uncorrected measured wall pressures along the vertical tail (sections *F–I*).

again the corrected experimental pressures are plotted for comparison. The figure shows that there is reasonable agreement between the experimental and computed pressure values. As expected, the surface pressure on the horizontal plate decreases with increasing distance from the vertical wall. Likewise, the wall pressure decreases with increasing distance from the leading edge as the shock-shock intersections moves farther away from both plates. Similar trends are seen in Fig. 18, which show wall pressure distributions on the vertical plate along sections *F*, *G*, *H*, and *I*. Once again the corrected pressures are plotted. There is good agreement between the measured pressures and the simulation results.

Simulation of the Control Jet-Interaction

The final calculation discussed in this paper is a simulation of a control-jet interaction as performed in the ESA wind-tunnel experiment. For this simulation, the exit plane of the jet coincided with the horizontal plate of the test model, and it was located 60 mm from the leading edge and 15 mm from the vertical wall (see Fig. 11). The jet itself was modeled as a drifting Maxwellian stream with a radially varying streaming velocity. The density of the incoming stream was constant across the exit plane of the nozzle; however, the total mass flux was equal to the mass flux predicted by VNAP2 (3.025×10^{-5} kg/s). In addition, the variable axial velocity and

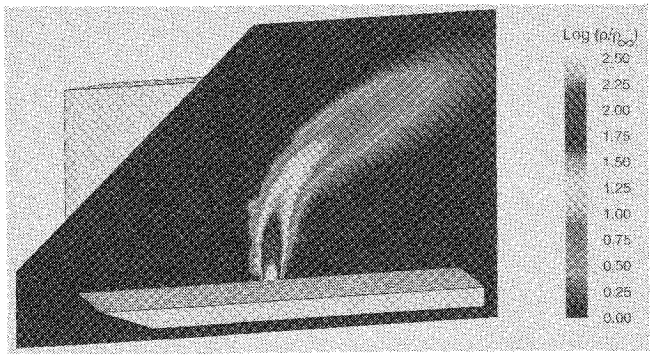

Fig. 19 Density of the jet species in the plane of the jet.

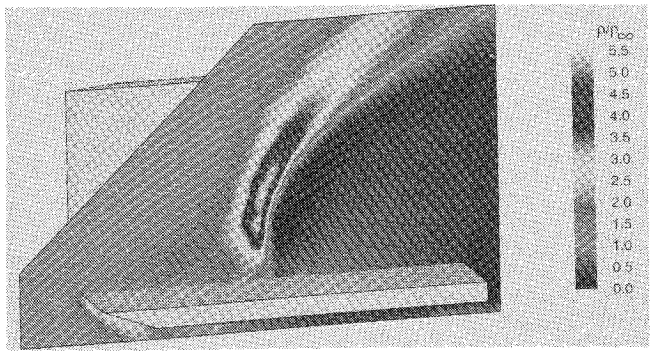

Fig. 20 Density of the freestream gas species in the plane of the jet.

temperature profiles computed with VNAP2 were preserved, since each incoming molecule was emitted with a velocity and temperature that was a function of the radius of the nozzle exit plane. It was assumed that the molecules entered with a velocity that was normal to the exit plane.

The three-dimensional computation used 900,000 particles and required 80 h on a Sun SPARCstation 10. The long computation time associated with this simulation was due to the high-density conditions in the core of the jet. It was possible for some cells in the core region of the jet to have molecules that collided thousands of times per time step. The effect of a single particle undergoing such a large number of collisions is to orient its thermal velocity vector in a random direction, thus placing the molecule in equilibrium with the rest of the molecules in the cell. Therefore, by limiting the number of collisions that can take place in a cell per time step to some multiple of the number of molecules in that cell, the computation time can be reduced significantly without a loss of accuracy. In this simulation, it was necessary to limit the number of possible collisions in the core of the jet to 100 times the number of molecules in each cell. This amounted to limiting collisions in 0.5% of cells in the entire computational domain. These cells were located in the jet core and were much larger than a mean free path. However, they were small compared with local density-gradient scales.

In this simulation the jet and freestream gases were both nitrogen, but for the purpose of analysis each gas was treated as a separate species with identical properties. This enabled the jet and freestream molecules to be tracked separately and their effect on the full flowfield to be determined. Figure 19 shows the density of the jet species. It can be observed that the external flow had little effect on the jet core, but it did significantly bend the outer part of the plume. The effect of the jet on the freestream flow is seen in Fig. 20, where the density of the freestream gas is shown. The jet appears to act as a barrier to the external flow, pushing the flow away and causing the freestream density to increase in front of the jet. Consequently, a low-density region is created immediately behind the jet, since the freestream molecules are effectively prevented from reaching that part of the flowfield. The overall flowfield can be seen in Fig. 21, which shows the combined density of the jet and external flow at several axial locations along the test model. The plane containing the jet shows the extent of the plume flowfield in the spanwise direction. An increase in density is evident between the jet and the

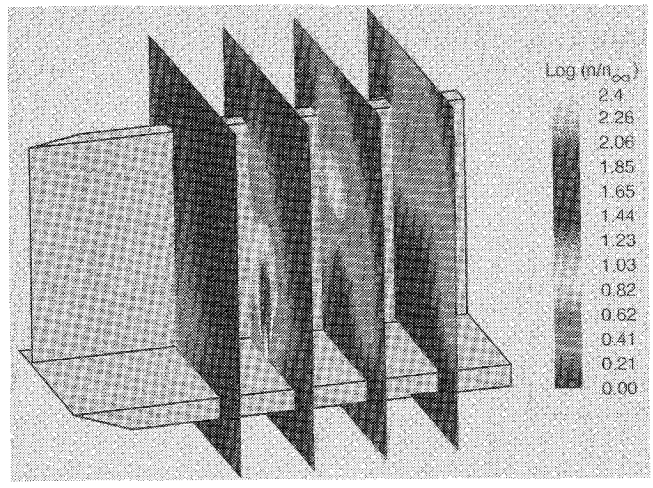

Fig. 21 Combined jet and freestream density contours at four axial locations.

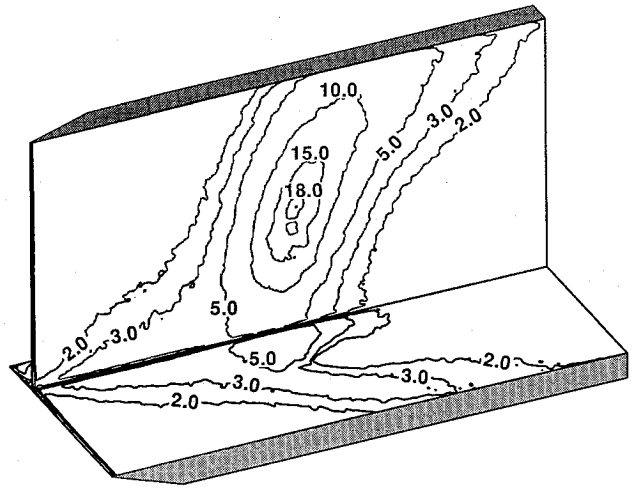

Fig. 22 Effect of the control-jet interaction on the computed surface pressure distribution along the test model.

vertical wall. It is apparent that there was little or no direct impingement of the jet on any of the surrounding surfaces. Therefore, any difference in the flowfield or surface properties from the undisturbed case was mainly due to the interaction of the jet with the external flow. The surface pressure distribution on both plates is shown in Fig. 22. The highest pressures occurred on the vertical wall. Lower pressures were recorded on the horizontal wall, the highest pressures there occurring just ahead of the jet. The surface pressure decreased behind the jet, since the external flow was practically blocked from reaching that part of the plate.

For the case of full jet interaction, experimental pressure measurements were taken along the sections of the test model shown in Fig. 11, using the same measurement technique that was used for the undisturbed corner flow. Likewise, the pressure measurements were corrected for orifice effects in the same way as the previous corner-flow calculation. These corrections were made assuming full energy accommodation and an orifice temperature of 300 K. Figure 23 compares the computed surface pressures with the corrected experimental values along section A. The jet was located on this section 60 mm from the leading edge. The computed and corrected experimental surface pressures from the undisturbed corner flow are also shown along section A to demonstrate the effect of the jet on the surface pressure. Both the computed and experimental results indicate that the jet increased the pressure ahead of it and caused the pressure to drop behind it. This is consistent with Fig. 20, which shows the freestream flow building up in front of the jet and being prevented from reaching the area behind the jet. The computed results agree

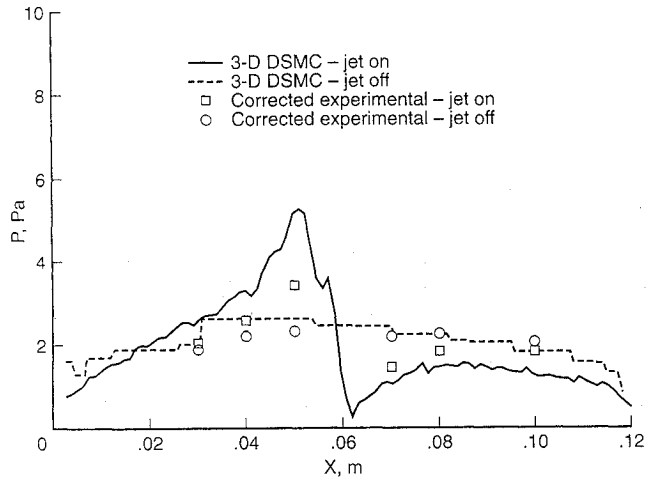

Fig. 23 Summary of the computed and corrected measured pressures along section *A* for the jet-on and jet-off cases.

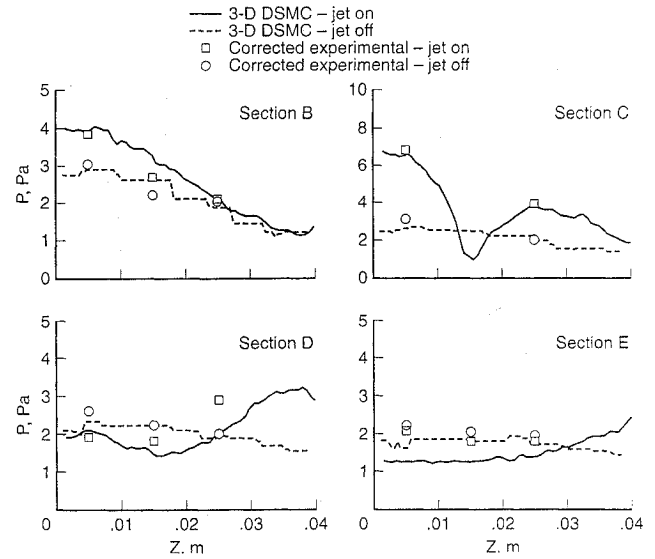

Fig. 24 Summary of the computed and corrected measured pressures along the horizontal plate for the jet-on and jet-off cases (sections *B–E*).

reasonably well with the experimental measurements except at the peak surface pressure. Also, the computed solution matches the trends seen in the experimental data.

Figure 24 shows the computed and corrected experimental surface pressure distributions on the horizontal plate along sections *B*, *C*, *D*, and *E*. Note that the jet is located on section *C*, 0.015 m from the wall. The computational results indicate the same trends seen in the experimental data. The computed pressures are in somewhat poor agreement with the experimental values, but the agreement is improved with the orifice corrections. The results show that the jet raises the pressure in section *B* ahead of the jet and section *C* on both sides of the jet. This is due to the barrier effect of the jet, which produces a buildup of the freestream flow in front of and on the sides of the jet. Similarly, sections *D* and *E* indicate lower pressures behind the jet, which result because most of the freestream flow is prevented from reaching those areas. The surface pressure distributions for the vertical plate are shown in Fig. 25 along sections *F*, *G*, *H*, and *I*. There is reasonable agreement between the computed and corrected experimental surface pressures, although there are large differences in section *G*, where the highest surface pressures occur. Also, the pressure peaks seem to differ in sections *H* and *I*. The jet-wall interaction effect is qualitatively correct, however, and the computed results show the same overall trends seen in the experimental data. The domain of influence of the jet can be seen by comparing the computed surface pressures with those of the undisturbed corner flow. The locations of the pressure peaks in sections *G*, *H*, and *I* correspond to the bending of the jet shown

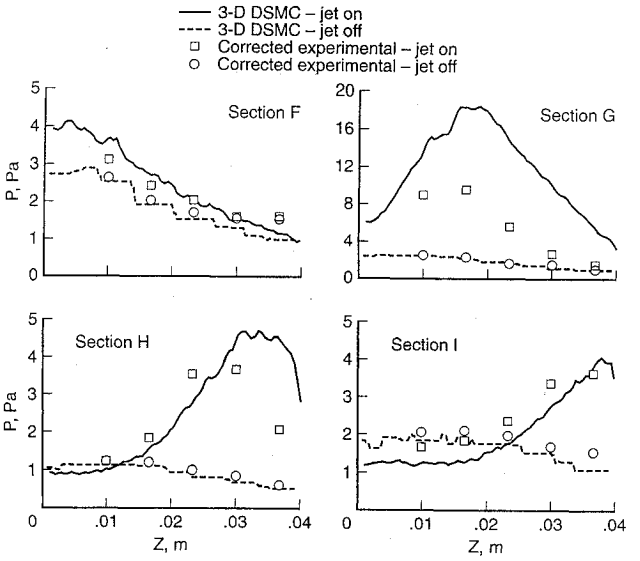

Fig. 25 Summary of the computed and corrected measured pressures along the vertical plate for the jet-on and jet-off cases (sections *F–I*).

in Fig. 19. Also, in Fig. 25 it is apparent that for the lower portions of the vertical wall the jet increases the surface pressure in the sections near the leading edge and lowers the pressure in the sections closer to the trailing edge. Once again, this is due to the displacement of the external flow ahead of the jet and the blockage of the freestream behind it.

Conclusions

In this study, a systematic approach has been developed for the numerical simulation of an ESA experiment involving a control-jet interaction with a low-density flow. Calculations were performed on several relevant subproblems in order to develop the best methodology for solving the full interaction problem. First, continuum (VNAP2) and noncontinuum (DSMC) methods were used in RCS nozzle and plume flow simulations, and the results from each method were compared with appropriate experimental data. The continuum and DSMC results matched well in the continuum portions of the nozzle flowfield. In addition, the DSMC results provided a good match to the experimentally measured pitot pressures in the nozzle exit plane and plume. These results were used as a guide to simulate the nozzle and plume flow of the jet from the ESA experiment. Next, the results from a three-dimensional DSMC code were compared with those generated with a well-established two-dimensional DSMC code for the case of a zero-incidence flat plate at the experimental flow conditions. Flowfield results generated with the two codes matched reasonably well except for the peak densities, which differed by 10%. Additionally, a three-dimensional DSMC simulation was performed on the undisturbed experimental test model, that is, without the jet firing. The results from this calculation compared well with experimental pressure measurements, especially when an orifice correction factor was applied to the experimental data. Finally, a simulation of the full ESA experiment with the jet turned on was performed with a three-dimensional DSMC code. In this simulation the jet was modeled as a uniform drifting Maxwellian stream with a variable velocity profile obtained from the previous continuum solution of the ESA nozzle. The number of collisions in the cells of the jet core region (0.5% of cells in the computational domain) were limited so that a solution could be obtained in a reasonable amount of time. The results indicated that the jet was significantly affected by the external flow, and this produced substantial changes in the surface pressure distribution across the entire test model. Reasonable agreement is seen between the predicted surface pressures and the experimentally measured results in most areas of the test model. However, there were significant differences between the computed and experimental results in the regions with the largest surface pressure changes. Although there were discrepancies in the specific surface pressure values, the computed pressures did exhibit similar trends to those indicated by the

experimental measurements. The discrepancies between the experimental and DSMC results may be diminished with improvements in the modeling of the jet inflow boundary condition. This may include coupling a DSMC simulation with a continuum solution of the high-density portion of the interaction region.

Acknowledgment

The authors would like to thank J. Leith Potter for his contributions with regard to the orifice corrections that were applied to the experimentally measured surface pressures.

References

[1]Kanipe, D. B., "Plume/Flowfield Jet Interaction Effects on the Space Shuttle Orbiter During Entry," AIAA Paper 82–1319, Aug. 1982.

[2]Allegre, J., Raffin, M., and Caressa, J. P., "Experimental Investigation of Transverse Jet Effects Related to Hypersonic Space Vehicles," *Aerothermodynamics for Space Vehicles*, ESA SP-318, May 1991, pp. 165–170.

[3]Romere, P. O., Kanipe, D. B., and Young, I. C., "Space Shuttle Entry Aerodynamic Comparison of Flight 1 with Preflight Predictions," *Journal of Spacecraft and Rockets*, Vol. 20, No. 1, 1983, pp. 15–21.

[4]Cline, M. C., "VNAP2: A Computer Program for Computation of Two-Dimensional, Time-Dependent, Compressible, Turbulent Flow," Los Alamos Scientific Laboratory, LA-8872, Los Alamos, NM, Aug. 1981.

[5]Bird, G. A., *Molecular Gas Dynamics*, Clarendon Press, Oxford, England, UK, 1976.

[6]Bird, G. A., "Monte-Carlo Simulation in an Engineering Context," *Rarefied Gas Dynamics*, edited by S. S. Fisher, Vol. 74, Progress in Astronautics and Aeronautics, AIAA, New York, 1981, pp. 239–255.

[7]Borgnakke, C., and Larsen, P. S., "Statistical Collision Model for Monte Carlo Simulation of Polyatomic Gas Mixture," *Journal of Computational Physics*, Vol. 18, No. 4, 1975, pp. 405–420.

[8]Bird, G. A., "The G2/A3 Program System Users Manual," G.A.B. Consulting Pty. Ltd., Killara, New South Wales, Australia, March 1992.

[9]Bird, G. A., "Application of the Direct Simulation Monte Carlo Method to the Full Shuttle Geometry," AIAA Paper 90-1962, June 1990.

[10]Rault, D. F. G., "Aerodynamics of High Altitude Reentry Shuttle Orbiter," AIAA Paper 93-2815, July 1993.

[11]Boyd, I. D., Penko, P. F., and Meissner, D. L., "Numerical and Experimental Investigations of Rarefied Nozzle and Plume Flows of Nitrogen," AIAA Paper 91-1363, June 1991.

[12]Penko, P. F., Boyd, I. D., Meissner, D. L., and DeWitt, K. J., "Pressure Measurements in a Low Density Nozzle Plume for Code Verification," AIAA Paper 91-2110, June 1991.

[13]Penko, P. F., Boyd, I. D., Meissner, D. L., and DeWitt, K. J., "Measurement and Analysis of a Small Nozzle Plume in a Vaccum," AIAA Paper 92-3108, July 1992.

[14]Boyd, I. D., Penko, P. C., Meissner, D. L., and DeWitt, K. J., "Experimental and Numerical Investigations of Low-Density Nozzle and Plume Flows of Nitrogen," *AIAA Journal*, Vol. 30, No. 10, 1992, pp. 2453–2461.

[15]Shapiro, A. H., *The Dynamics and Thermodynamics of Compressible Fluid Flow*, Ronald Press, New York, 1953.

[16]Bird, G. A., "Breakdown of Transitional and Rotational Equilibrium in Gaseous Expansions," *AIAA Journal*, Vol. 8, No. 11, 1970, p. 1998.

[17]Allegre, J., and Raffin, M., "Experimental Study on Control-Jet/Corner-Flow Interaction," SESSIA, 1759/92.1133, Meudon, France, Nov. 1992.

[18]Potter, J. L., and Blanchard, R. C., "Thermomolecular Effect on Pressure Measurements with Orifices in Transitional Flow," *Proceedings of the 17th International Symposium on Rarefied Gas Dynamics*, Aachen, Germany, 1990, pp. 1459–1465.